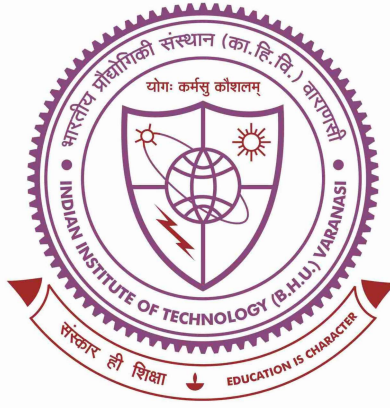


# **Impact of long- and short-range atomic ordering on the functional properties of Sodium Niobate based ceramics**



**Thesis submitted in partial fulfillment  
for the Award of  
DOCTOR OF PHILOSOPHY  
in  
PHYSICS**

*by*  
**HARSH KUMAR**

*Under the supervision of*  
**Dr. Saurabh Tripathi**

**DEPARTMENT OF PHYSICS  
INDIAN INSTITUTE OF TECHNOLOGY  
BANARAS HINDU UNIVERSITY  
VARANASI - 221 005**

**ROLL NUMBER**  
19171002

**YEAR OF SUBMISSION**  
2025

*Dedicated to my mother*

## Certificate

It is certified that the work contained in the thesis titled **“Impact of long- and short-range atomic ordering on the functional properties of Sodium Niobate based ceramics”** by **Mr. Harsh Kumar**, Roll Number **19171002**, has been carried out under my supervision, and this work has not been submitted elsewhere for a degree.

It is further certified that the student has fulfilled all the requirements of the Comprehensive Examination, Candidacy, and SOTA for the award of **Ph.D. Degree in Physics**.

Date: 27/06/2025

Place: IIT (BHU), Varanasi

*Saurabh Tripathi*

**Signature:**

**Supervisor**

Dr. Saurabh Tripathi

(Associate Professor)

Department of Physics

Indian Institute of Technology (BHU),

Varanasi-221005 (U.P.), India

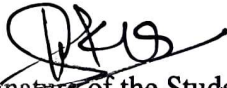
Associate Professor  
Department of Physics  
Indian Institute of Technology  
(Banaras Hindu University)  
Varanasi-221005

## Declaration

I, **Harsh Kumar**, certify that the work embodied in this thesis is my own bona-fide work and carried out by me under the supervision of **Dr. Saurabh Tripathi** from July 2019 to June 2025 at the **Department of Physics, Indian Institute of Technology (BHU), Varanasi**. The matter embodied in this thesis has not been submitted for the award of any other degree/diploma. I declare that I have faithfully acknowledged and given credit to the research workers whenever and wherever their works have been cited in my work in this thesis. I further declare that I have not wilfully copied any others' work, paragraphs, text, data, results, etc., reported in journals, books, magazines, reports dissertations, theses, etc., or available at websites and have not included them in this thesis and have not cited as my own work.

Date: 27/06/2025

Place: IIT (BHU), Varanasi

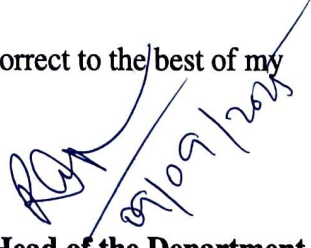
  
Signature of the Student  
(Harsh Kumar)

---

## Certificate by the Supervisor

It is certified that the above statement made by the student is correct to the best of my knowledge.

  
Signature: Supervisor  
(Dr. Saurabh Tripathi)  
Associate Professor  
Department of Physics  
Indian Institute of Technology  
(Banaras Hindu University)  
Varanasi-221005

  
Signature of the Head of the Department  
HEAD/विभागाध्यक्ष  
भौतिकी विभाग/Deptt. of Physics  
भा०प्रौ०सं०/(का०हि०वि०)/IIT (BHU)  
वाराणसी/Varanasi-221005

# Copyright Transfer Certificate


**Title of the Thesis :** Impact of long- and short-range atomic ordering on the functional properties of Sodium Niobate based ceramics

**Name of the Student :** Harsh Kumar

## Copyright Transfer

The undersigned hereby assigns to the Indian Institute of Technology (Banaras Hindu University) Varanasi all rights under copyright that may exist in and for the above thesis submitted for the award of the **Doctor of Philosophy in Physics**.

Date: 27/06/2025

  
Signature of the Student

Place: IIT (BHU), Varanasi

(Harsh Kumar)

**Note: However, the author may reproduce or authorize others to reproduce material extracted verbatim from the thesis or derivative of the thesis for author's personal use provided that the source and the Institute's copyright notice are indicated.**

## Acknowledgements

*“Deeksha Sanskar” is a sacred Hindu ritual symbolizing the aspirant’s journey to Kashi in pursuit of knowledge, highlighting the timeless significance of the city as a center of learning. I feel truly blessed to have realized this tradition in its truest sense by residing in Kashi (modern-day Varanasi) to pursue the highest academic degree of my life, the “Doctor of Philosophy (Ph.D.)”. I express my heartfelt gratitude to Lord Mahadev for granting me the divine opportunity to live and learn in this holy city.*

I would like to begin by expressing my sincere gratitude to my supervisor, Dr. Saurabh Tripathi, for his invaluable guidance and unwavering encouragement throughout the course. I am thankful to him for addressing my ignorance, which pushed me to rectify my mistakes as much as possible. His enthusiasm and dedication towards the research have been vital for me during the challenging phases. Next, I want to thank my RPEC members, Prof. Sandip Chatterjee and Dr. Akhilesh Kumar Singh, for their constructive comments on my work. In addition, my thanks go to all faculty and non-teaching staff for their support during my tenure. I extend my appreciation to my collaborators, Dr. Sanjit Ghose (Brookhaven National Laboratory, USA), Dr. Rudolph Erasmus (University of Witswatersrand, South Africa), Dr. Jose Antonio Alonso (C.S.I.C., Spain), Dr. Jose Luis Martinez (C.S.I.C., Spain), Dr. Anar Singh (Lucknow University, India), and Dr. Akhilesh Kumar Singh (IIT BHU, India), for their assistance with various measurements and data interpretation. I acknowledge the Central Instrumental Facility at IIT(BHU) for providing access to the instrumental facilities. I owe thanks to my labmates Anuvrat Tripathi, Tanu Swami, Sanjeev Kumar, Kartikey Chaturvedi, and Ajay Singh for our insightful discussions on work-related topics, and to my senior, Dr. Digvijay Nath Dubey, for resolving my research-related queries.

My heartfelt thanks go to my mother, Mrs. Maya Devi Shukla, for her patience, encouragement, and unwavering support throughout my academic journey. I also appreciate my siblings, Mrs. Deeksha Dwivedi and Mr. Rishabh Kumar, for their endless love and support. An enormous debt is owed to my best friend and wife, Dr. Manisha, for her belief in me during my lowest phases and for motivating me to strive for excellence. Additionally, I am thankful to Mr. Vikash Dwivedi, Mr. Radhe Shyam, Mrs. Santosh Dixit, Ms. Komal Dixit, Mr. Sandeep Dixit, Mrs. Raveena, and Mr. Gourav Dixit for their moral support and advice.

I am grateful to my friends Pawan Kumar Mishra, Ashish kumar Singh, Anuvrat Tripathi, Sachin Singh, Santosh Kacchap, Sourav Chandra, Kaustubh Naik, Shubham Garg, Bhagyashree Verma, Neha Patel, Shweta Didel, Samiksha Shrivastav, and Akanksha Gautam for creating an energetic environment that helped ease work-related stress. Special thanks to Dr. Ashish Choksey and the Scholars' Cricket Committee for maintaining cricket activities, which are crucial for mental and physical health.

I acknowledge the financial assistance from the Science and Engineering Research Board (SERB) for providing a travel grant to attend the International Conference in Kyoto, Japan. I am also indebted to the Indian Institute of Technology (BHU) for funding my Ph.D. research.

Finally, I want to sincerely thank Almighty God for guiding me throughout this journey and for all the blessings and strength I have received along the way.

**Harsh Kumar**

# List of tables

1.1	Wyckoff sites occupied by atoms in low- and high-symmetry structures, along with phonon modes responsible for symmetry breaking. . . . .	20
1.2	Space Group of RFeO <sub>3</sub> compounds with corresponding references. . . . .	24
3.1	Structural parameters, phase fraction, and various agreement factors obtained from the Rietveld refinements of the X-ray diffraction patterns for $x=0.01$ via two-phase ( $Pbcm+Pmc2_1$ ) coexistence model. . . . .	80
3.2	Structural parameters, phase fraction, and various agreement factors obtained from the Rietveld refinements of the X-ray diffraction patterns for $x=0.10$ via two-phase ( $Pmc2_1+Am2$ ) coexistence model. . . . .	81
4.1	Various models used for fixing the diffraction pattern along with their temperature range in heating and cooling cycles. . . . .	109
4.2	Structural parameters, phase fraction, and various agreement factors for NN-10BCT obtained from the Rietveld refinements of the Synchrotron X-ray diffraction pattern at 8 K using two-phase ( $R3c+Pmc2_1$ ) coexistence model. . . . .	109
4.3	Structural parameters, phase fraction, and various agreement factors for NN-10BCT obtained from the Rietveld refinements of the Synchrotron X-ray diffraction pattern at 250 K using $Pmc2_1$ model. . . . .	110

---

4.4	Structural parameters, phase fraction, and various agreement factors for NN-10BCT obtained from the Rietveld refinements of the Synchrotron X-ray diffraction pattern at 300 K using two-phase ( $Pmc2_1 + Amm2$ ) coexistence model. . . . .	111
4.5	Structural parameters, phase fraction, and various agreement factors for NN-10BCT obtained from the Rietveld refinements of the Synchrotron X-ray diffraction pattern at 390 K using $Amm2$ model. . . . .	112
4.6	Structural parameters, phase fraction, and various agreement factors for NN-10BCT obtained from the Rietveld refinements of the Synchrotron X-ray diffraction pattern at 470 K using $P4bm$ model. . . . .	114
4.7	Structural parameters for PDF analysis performed using a two-phase coexistence model ( $Cc + Pmc2_1$ ) at 8 K. A similar model was employed to fit PDF profiles at various temperatures. The model used for fitting the PDF profiles with the $R3c + Pmc2_1$ phase coexistence model is similar to the model shown in Table 4.2. . . . .	121
5.1	Structural parameters and agreement factors for NN-25BCT obtained from the Rietveld refinements of the Synchrotron X-ray diffraction pattern at various temperatures using $P4bm$ model. . . . .	134
5.2	Structural parameters and agreement factors for NN-25BCT obtained from the Rietveld refinements of the Synchrotron X-ray diffraction pattern at various temperatures using $P4/mbm$ model. . . . .	135
5.3	Structural parameters, and agreement factors for NN-25BCT obtained from the Rietveld refinements of the Synchrotron X-ray diffraction pattern at various temperatures using $Pm\bar{3}m$ model. . . . .	136

- 
- 5.4 Wyckoff site splitting in high- and low-symmetry structures with corresponding symmetry-breaking modes. Here, A and B represent the atoms positioned at the A and B sites of the perovskite structure. . . . . 137

# List of figures

1.1	The relationship between the piezoelectric, pyroelectric, and ferroelectric materials. . . . .	4
1.2	Representation of direct and converse piezoelectric effect. . . . .	6
1.3	Potential energy curve for a ferroelectric material. . . . .	9
1.4	Polarization vs. electric field (PE) hysteresis loop for a normal ferroelectric, having the remnant polarization ( $P_r$ ) and coercive field ( $E_c$ ). . . . .	10
1.5	The representation of the unit cell of an ideal cubic perovskite ( $ABO_3$ ) structure. . . . .	11
1.6	Illustration of different octahedral tilting. The left column shows $a^0a^0a^0$ (no tilt), the middle column shows $a^0a^0c^-$ (out-of-phase tilting), and the right column shows $a^0a^0c^+$ (in-phase tilting). The upper (lower) row shows the structures in the $xy$ -plane ( $zx$ -plane); adopted from [1]. . . . .	16
1.7	Schematic representation of the atomic displacement pattern of various distortion modes involved in the symmetry-breaking transition $Pm\bar{3}m \rightarrow Pbnm$ : (a) $R_5^+$ (Eu), (b) $R_5^+$ (O), (c) $X_5^+$ (Eu), (d) $X_5^+$ (O), (e) $R_4^+$ , (f) $M_3^+$ , (g) $M_2^+$ . Irreducible representations affecting more than one atom ( $X_5^+$ and $R_5^+$ ) are represented separately. . . . .	21

1.8	Temperature-dependent evolution of $X_5^+$ (Eu) and $R_5^+$ (Eu) phonon mode amplitudes. These two modes are responsible for the displacement of the Eu atom from its position in an ideal cubic structure. . . . .	22
1.9	Evolution of amplitude of various phonon modes as a function of R cationic radii. . . . .	23
1.10	Schematic representation of polymorphic phase boundary (PPB) and morphotropic phase boundary (MPB) existing between two ferroelectric phases, $F_1$ and $F_2$ . . . . .	26
1.11	Morphotropic phase boundary in $\text{Pb}(\text{Zr},\text{Ti})\text{O}_3$ [2] . . . . .	28
1.12	Schematic representation of polar directions in monoclinic $M_A$ , $M_B$ , and $M_C$ phases [3]. . . . .	29
1.13	Schematic representation of dielectric permittivity behaviour exhibited by relaxor ferroelectrics [4]. . . . .	30
1.14	Polar nano regions in a non-polar matrix. . . . .	31
1.15	Schematic representation of polar nano-regions in the cubic matrix [5]. . . . .	32
1.16	Phase evolution of $\text{NaNbO}_3$ with temperature. The figure is adopted from ref. [6] . . . . .	36
1.17	Variation of real part of dielectric permittivity of barium titanate as a function of temperature [7]. . . . .	37
1.18	Schematic representation of off-centered Ti atom along $\langle 111 \rangle$ directions in (a) rhombohedral, (b) orthorhombic, (c) tetragonal, and (d) cubic phases of $\text{BaTiO}_3$ [8]. . . . .	39
1.19	(a) Phase diagram of $\text{BaTiO}_{3-x}\text{CaTiO}_3$ ceramics [9], (b) representation of off-centered calcium atoms in the tetragonal phase of $\text{BaTiO}_{3-x}\text{CaTiO}_3$ [10], and (c) the relative energies of $\text{BaTiO}_{3-x}\text{CaTiO}_3$ ; $x = 0.125$ for off-centered Ca atoms along [001], [111], and [113] directions [10]. . . . .	41

---

2.1	The instruments used in the synthesis of samples via the solid-state reaction method. . . . .	47
2.2	Representation of X-ray diffraction by a crystal. . . . .	49
2.3	Rigaku SmartLab high-resolution X-ray diffractometer. . . . .	50
2.4	The National Synchrotron Light Source II (NSLS-II), Brookhaven National Lab, US . . . . .	54
2.5	WITec Raman Microscope alpha300R . . . . .	57
2.6	LCR meter along with variable temperature stage for dielectric measurements. . . . .	59
2.7	Polarization vs. electric field (PE) hysteresis loop tracer (Radiant Inc.). . .	62
2.8	Schematic illustration of dipoles, domain structures and polarization hysteresis loops for linear dielectrics, ferroelectrics, relaxor ferroelectrics and antiferroelectric materials. The figure is adopted from [11]. . . . .	63
2.9	High-resolution scanning electron microscope. . . . .	65
3.1	Scanning electron micrographs and grain size distribution plots of the sintered pellets of NN- $x$ BCT ceramics for $x=0.01, 0.10, 0.15,$ and $0.25$ . . .	73
3.2	Composition dependent powder X-ray diffraction profile of NN- $x$ BCT for $0.00 \leq x \leq 0.25$ . The Bragg reflections have been indexed with respect to a doubled perovskite cell. . . . .	74
3.3	Evolution of superlattice reflections(left panel) and main perovskite reflections(right panel) with increasing BCT content. . . . .	75
3.4	Rietveld refined X-ray diffraction (XRD) patterns of NN- $x$ BCT for a few representative compositions. . . . .	79
3.5	Variation of (a) lattice parameters, (b) volume of the elementary cell. (Inset shows the evolution of monoclinic angle for composition with pseudo-monoclinic basic cell). . . . .	80

3.6	Polarization vs Electric field(P-E) for some representative composition at 25 kV/cm and at a frequency of 10 Hz. The inset shows the remanent polarization as a function of composition. . . . .	82
3.7	Composition-dependent real and imaginary part of dielectric permittivity measured at 10 kHz. . . . .	83
3.8	Temperature dependent real part of dielectric permittivity for $x = 0.25$ at 10 kHz (a) frequency dependence of real part of dielectric permittivity (b) fitting of modified Curie-Weiss law (c) Diffusivity. . . . .	84
3.9	Room temperature Raman spectra of NN- $x$ BCT for different compositions. All the Raman spectra have been deconvoluted using a suitable number of Lorentz peaks. The Raman mode marked around $93 \text{ cm}^{-1}$ for $x = 0$ (i.e., $\text{NaNbO}_3$ ) is linked to the T point instability of the cubic Brillouin zone. The appearance of a broad band around $150 \text{ cm}^{-1}$ marks the phase transition $Pmc2_1$ ( $0.02 \leq x \leq 0.06$ ) $\rightarrow$ $Amm2$ ( $x = 0.15$ ) via coexistence of two ferroelectric phases for $x = 0.08$ & $0.10$ . This band disappears for $x > 0.15$ , indicating another phase transition to $P4bm$ . . . . .	87
3.10	Composition-dependent evolution of X-ray diffraction profiles of $\{200\}_{\text{pc}}$ , $\{220\}_{\text{pc}}$ , and $\{222\}_{\text{pc}}$ perovskite reflections of NN- $x$ BCT for $0.30 \leq x \leq 1.0$ . . . . .	89
3.11	Temperature dependent dielectric permittivity of NN- $x$ BCT ceramics at several frequencies for $x = 0.40, 0.60,$ and $0.80$ . . . . .	90
3.12	Le-bail Refined X-ray diffraction pattern of NN- $x$ BCT for a few representative compositions. Inset shows the refinement fitting for $\{200\}_{\text{pc}}$ , $\{220\}_{\text{pc}}$ , and $\{222\}_{\text{pc}}$ perovskite reflections. . . . .	92
3.13	Composition dependent P-E loops for NN- $x$ BCT for $0.50 \leq x \leq 0.80$ . . .	93
3.14	Composition dependent Raman spectra of NN- $x$ BCT for $0.30 \leq x \leq 1.0$ .	96

- 
- 4.1 Temperature dependent (a) real and (b) imaginary part of dielectric permittivity in a wide temperature range of 100 K-600 K.(c) Derivative of the real part of dielectric permittivity with respect to temperature marking the weak phase transition around 200 K and 130 K during the heating and cooling cycle respectively. (d) The inverse of dielectric permittivity is plotted against the temperature. The inset shows the frequency-independent dielectric maxima, which is a feature of classical ferroelectric material. . . . . 104
- 4.2 Evolution of Main perovskite reflections *viz.*,  $\{400\}_{\text{dpc}}$ ,  $\{440\}_{\text{dpc}}$  and  $\{444\}_{\text{dpc}}$  as well as superlattice reflections in (a) Heating (b) Cooling cycle. The shaded rectangle shows the appearance of a new peak beside the  $\{444\}_{\text{dpc}}$  reflection around 190 K and 130 K during the heating and cooling cycles, respectively. The dashed rectangle shows the changes in the main perovskite reflections around room temperature. . . . . 106
- 4.3 Rietveld refined X-ray diffraction (XRD) patterns of NN-10BCT for a few representative temperatures. The red circles show the observed diffraction data, while the black line shows the simulated pattern. The blue line is the difference between observed and simulated patterns. Inset shows the fitting around the superlattice reflections and main perovskite reflections. 107
- 4.4 Raman spectra of NN-10BCT at different temperatures in the range of 100-650 K. The Raman spectra have been taken during the heating cycle using the protocol described in the experimental section. All the Raman spectra have been deconvoluted using a suitable number of Lorentz peaks. 113
- 4.5 Temperature evolution of the wave number (Raman shift) of stretching Raman mode around  $600\text{ cm}^{-1}$ . . . . . 114

- 
- 4.6 Experimental Variable temperature  $G(r)$  for  $r \approx 1-10 \text{ \AA}$  for  $0.9\text{NaNbO}_3-0.1\text{Ba}_{0.9}\text{Ca}_{0.1}\text{TiO}_3$  ceramic powders in (a) Heating (b) Cooling modes, showing the evolution of short-range structures (c) Experimental  $G(r)$  within  $\approx 4 \text{ \AA}$ , showing the nearest neighbour pairwise atomic correlations. (d)  $G(r)$  depicting the length of structural coherence at some representative temperatures . . . . . 118
- 4.7 Refinement of PDF profile for different length scale at 8 K using (a)-(d)  $\text{Cc}+\text{Pmc}2_1$  model & (e)-(h)  $R3c+\text{Pmc}2_1$  models. PDF refinement with  $\text{Cc}+\text{Pmc}2_1$  model for  $1.7 \leq r \leq 10 \text{ \AA}$  at different temperatures *viz.*, 50K, 250 K, and 490 K have been shown in (i), (j), and (k), respectively. . . . . 120
- 5.1 (a) Temperature-dependent evolution of real and imaginary part of dielectric permittivity.(b) Vogel-Flucher fitting of the temperatures corresponding to the dielectric to estimate the freezing temperature. (c) The inverse of dielectric permittivity as a function of temperature marks the Burns Temperature. . . . . 130
- 5.2 Temperature-dependent evolution of (a) superlattice reflections, (b)-(d) main perovskite reflections. Evolution of (e) lattice parameters, (g) volume of the elementary cell, and (f) tetragonality of the elementary cell as a function of temperature. . . . . 132
- 5.3 Rietveld Refinement fit of the diffraction pattern at 500 K, 300 K, and 110 K using the  $\text{Pm}\bar{3}m$ ,  $\text{P}4/\text{mbm}$ ,  $\text{P}4\text{bm}$  space group, respectively. The inset shows the fitting around the main perovskite peaks and superlattice reflections. . . . . 133

- 
- 5.4 Temperature-dependent evolution of (a)  $M_3^+$  and (b)  $\Gamma_4^-$  modes in the stability region of long-range ferroelectric phase with  $P4bm$  space group calculated using the information obtained from refinement of SXRD patterns. . . . . 137
- 5.5 Room temperature polarization vs electric field (P-E) and associated current vs electric field (I-E) loops of NN-25BCT measured at a maximum electric field of 20 kV/cm. The slim hysteresis loop is characteristic of a relaxor-like behaviour. . . . . 139
- 5.6 Variable temperature Raman spectra of NN-25BCT in the temperature range  $100 \leq T \leq 850$  K. The Raman spectra have been taken during the heating cycle using the protocol described in the experimental section. . . 140
- 5.7 Deconvoluted Raman spectra of NN-25BCT at some representative temperatures. All the Raman spectra have been fitted using a suitable number of Lorentz peaks. . . . . 141
- 5.8 Temperature-dependent variation of the FWHM of the Raman mode located near  $250 \text{ cm}^{-1}$ . The black dashed line is a polynomial baseline to account for the trivial decrease in phonon widths on heating. . . . . 142
- 5.9 (a) Temperature dependent evolution of PDF profiles of NN-25BCT. Atomic PDF fitting at 500 K using different plausible models *viz.*, (b)  $Pm\bar{3}m$ (c)  $P4/mbm$ , (d)  $P4mm$ , (e)  $P4bm$ . The goodness of fit parameter suggests that the  $P4bm$  model produces the best fit to the data. . . . . 144
- 5.10 The experimental (red dots) and calculated (black continuous line) pair distribution functions (PDFs) and their difference (blue line at the bottom) using the tetragonal space group ( $P4bm$ ) in the temperature range 110 - 450 K obtained by refinement using the PDFgui program. . . . . 145

5.11	Temperature dependent evolution of $\Gamma_4^-$ mode calculated for short-range ordering(SRO) using the information obtained from refinement of PDF patterns. . . . .	146
6.1	(a) Temperature-dependent evolution of real and imaginary part of dielectric permittivity, (b) The inverse of the dielectric permittivity as a function of temperature marks the Burns Temperature,(c) linear fitting of $\log(1/\epsilon' - 1/\epsilon'_m)$ vs. $\log(T - T_m)$ at 100 KHz (d) Vogel-Fulcher fitting of the temperatures corresponding to the dielectric to estimate the freezing temperature. . . . .	153
6.2	Temperature-dependent evolution of main perovskite reflections <i>viz.</i> , $\{200\}_{pc}$ , $\{220\}_{pc}$ , and $\{222\}_{pc}$ of NN-60BCT. . . . .	156
6.3	Le-Bail refined diffraction patterns of NN-60BCT at some representative compositions. The inset shows the fitting for $\{200\}_{pc}$ , $\{220\}_{pc}$ , and $\{222\}_{pc}$ main perovskite reflections. . . . .	158
6.4	Temperature-dependent variation of volume for the two cubic components present in NN-60BCT ceramic, where the symbol represents the experimental volume, the solid curve represents the polynomial fit of the experimental volume, and the black line represents the nominal volume obtained from the fitting of the Debye-Grüneisen equation for 100-500 K	159
6.5	Temperature-dependent variation of spontaneous volume ferroelectrostriction (SVFS) calculated for the two cubic components. . . . .	160
6.6	Temperature-dependent Raman spectroscopy data for NN-60BCT. . . . .	162
6.7	Temperature-dependent evolution of deconvoluted relative intensity of the Raman mode present around $\approx 305 \text{ cm}^{-1}$ . . . . .	164

- 
- 6.8 (a) Temperature-dependent evolution of experimental atomic PDFs of NN-60BCT. Correlation peaks arising from different bonds are marked using arrows. Fitting of the PDF profiles at 300 K using (b)  $R3m$ , (c)  $P4bm$ , and (d)  $R3m+P4bm$  models along with their goodness of fit parameters. . . . 165
- 6.9 PDF fitting of NN-60BCT using the two-phase ( $R3m+P4bm$ ) model shown at some representative temperatures along with goodness of fit parameters. 166
- 6.10 Evolution of PNRs in NN-60BCT as a function of temperature. The red and turquoise blue are the rhombohedral and tetragonal PNRs, embedded in BT-like ( $C_{BT}$ ) and NN-like ( $C_{NN}$ ) in cubic matrices, respectively. . . . 167